aerospace

MDPI

Article

Wind Tunnel Investigation of Transient Propeller Loads for Non-Axial Inflow Conditions

Catharina Moreira [1,*], Nikolai Herzog [2] and Christian Breitsamter [1]

[1] Chair of Aerodynamics and Fluid Mechanics, Technical University of Munich, 85748 Munich, Germany; christian.breitsamter@tum.de
[2] Rolls-Royce Deutschland Ltd. & Co. KG, 15827 Dahlewitz, Germany; nikolai.herzog@rolls-royce-electrical.com
* Correspondence: catharina.moreira@tum.de

Abstract: Recent developments in electrical Vertical Take-off and Landing (eVTOL) vehicles show the need for a better understanding of transient aero-mechanical propeller loads for non-axial inflow conditions. The variety of vehicle configurations conceptualized with different propellers in terms of blade geometry, number of blades, and their general integration concept results in aerodynamic loads on the propellers which are different from those on conventional fixed-wing aircraft propellers or helicopter rotors. Such varying aerodynamic loads have to be considered in the vehicle design as a whole and also in the detailed design of their respective electric propulsion systems. Therefore, an experimental approach is conducted on two different propeller blade geometries and a varying number of blades with the objective to explore the characteristics at non-axial inflow conditions. Experimental data are compared with calculated results of a low-fidelity Blade Element Momentum Theory (BEMT) approach. Average thrust and side force coefficients are shown to increase with inflow angle, and this trend is captured by the implemented numerical method. Measured thrust and in-plane forces are shown to oscillate at the blade passing frequency and its harmonics, with higher amplitudes at higher angles of inflow or lower number of blades.

Keywords: propellers at incidence; non-axial inflow; aerodynamic loads; tiltrotor; wind tunnel; experimental aerodynamics; fixed-pitch propeller; BEMT; transient propeller loads

Citation: Moreira, C.; Herzog, N.; Breitsamter, C. Wind Tunnel Investigation of Transient Propeller Loads for Non-Axial Inflow Conditions. *Aerospace* **2024**, *11*, 274. https://doi.org/10.3390/aerospace11040274

Academic Editor: Alex Zanotti

Received: 29 February 2024
Revised: 27 March 2024
Accepted: 28 March 2024
Published: 30 March 2024

1. Introduction

The development of an innovative aircraft for Regional Air Mobility (RAM) and Urban Air Mobility (UAM) has been approached with increased interest in recent years. This has raised unique aircraft system and subsystem requirements. Several new vehicle solutions have been proposed to meet them: over 700 concepts by over 300 different companies have been included in the Vertical Flight Society database [1]. Some manufacturers are moving quickly through testing prototypes, manned flight, and even towards certification of new vehicles. Estimates suggest the UAM market could reach a value of USD 32B by 2035 [2].

From a technical perspective, recently proposed solutions for these vehicles incorporate characteristics from both fixed-wing aircraft and rotorcraft in order to combine the advantages of range and speed of the former with the maneuverability of the latter. Some of the proposed architectures for UAM vehicles introduce features such as distributed propulsion, propeller–wing configurations and wings or propellers that can be tilted in flight. However, many of the propulsion concepts are highly aerodynamically complex and diverge from traditional axial inflow operating conditions for propellers [3,4].

Some proposed vehicle architectures, such as tiltrotor aircraft, require a transition between vertical and horizontal flight and thus inevitably encounter non-axial inflow conditions during flight due to the reconfiguration of the propulsion system [2]. Other architectures for eVTOL aircraft have fixed orientation propellers to provide thrust and lift

individually, the so-called Lift+Cruise concepts [2]. These configurations have the advantage of reduced complexity for not requiring large scale in-flight reconfiguration of wings or propulsion systems. However, they may face integration issues due to the influence of lifter rotors still present in the flow during cruise flight, albeit shut down, which can affect not only vehicle drag but also performance of wings and active propulsion systems as well as the structure of the vehicle itself. Design parameters such as the number of blades can have a significant impact on the performance of a concept. Selecting a two-bladed or four-bladed propeller for the lifter rotors, for example, could enable the alignment of blades with oncoming airflow during cruise, but this selection also impacts the aerodynamic behavior of the rotor itself. In this scenario, it is clear that a detailed understanding of both averaged and time-resolved aerodynamic characteristics of propellers under non-axial inflow conditions, including their dependencies on not only operating conditions but also design parameters, such as number of blades, is crucial for the development of an eVTOL aircraft.

Previous experimental work was carried out in the early 20th century [5,6] focused on assessing changes in average forces and moments of propellers operating in yaw and their effect on aircraft stability. These studies reported not only changes in thrust and power coefficients and propeller efficiency, but also the observation that additional moments and in-plane forces arise from operation in non-axial inflow. Later, in the 1940s to 1960s, further experimental investigations [7–9] were conducted over wider ranges of angles of incidence. Also during this period, the theoretical modeling of propeller loads at incidence was advanced [10,11]. There has been renewed interest on the topic in the last decade, possibly motivated by the further development of UAV (Unmanned Aerial Vehicle) and eVTOL concepts, with several authors investigating average loads of propellers at incidence [12–15], while experimental results for loads in the frequency domain are scarce but have been reported in [16].

Experimental data are invaluable in order to validate existing prediction tools for the new conditions expected for an eVTOL aircraft or develop new prediction tools. This work aims to contribute to the aforementioned experimental database and expand it by including time-resolved load data to enable an analysis of oscillatory behavior induced by asymmetric inflow in addition to average loads.

2. Methodology

In this section, the experimental setup is introduced, including the electric motor, the load cell, the types of propellers being tested, and further components. The considered parameter space and measurement procedure are described. Then, the numerical approach is introduced with a short description of the used Blade Element Momentum Theory (BEMT) method, including selected parameters.

2.1. Experimental Approach

A test bench for an isolated small-scale propeller was developed to allow for the investigation of different propeller configurations and inflow conditions, including variations in rotational speed, blade geometry, number of blades, and Angle of Inflow (AoI). The experimental setup is based on previous work [17,18] and was adapted to enable time-resolved measurements and to focus on certain parameter variations, such as number of blades and blade pitch angle. The experimental setup can be seen in Figure 1.

The test bench consists of an outrunner brushless electric motor with a fixture for off-the-shelf propeller blades. The motor is connected to a six-component load cell used to measure time-resolved forces and moments. An insulating polytetrafluoroethylene (PTFE) disk was included between the motor and the load cell in order to hinder heat transfer between these components, since temperature changes at the load cell were observed to influence measurement results. Also due to this observation, a temperature sensor was attached to the load cell for monitoring purposes. Additionally, an optical sensor was included to enable measurements of the rotational speed of the motor. This approach was selected not only because it could be integrated easily with existing equipment, but also

because its small dimensions allow for flow disturbances induced by the inclusion of this sensor to be kept to a minimum. The optical sensor was placed in a custom 3D-printed support attached to the motor fixture and a reflective tape was placed on the motor itself such that the voltage peaks of the optical sensor caused by the reflective tape once per revolution could be used to calculate rotations per minute (RPM) for data analysis. The measurement equipment is supported by steel beams and placed on a rotating platform in the wind tunnel, which enables rotation of the entire test bench for adjustment of the inflow angle.

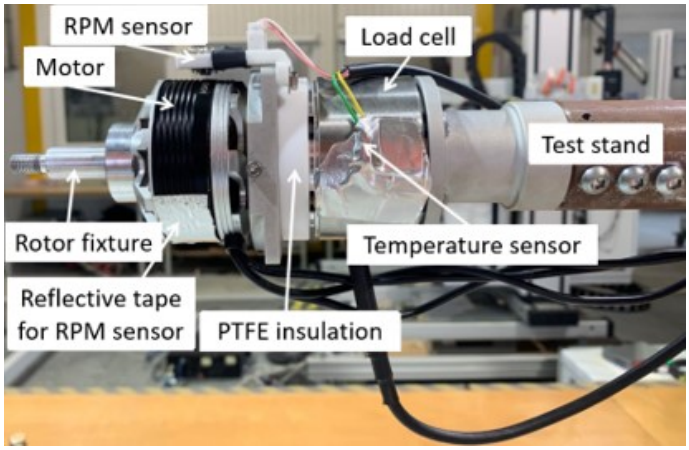

Figure 1. Components of the experimental propeller test bench for the wind tunnel campaign. Propeller blades (not shown on this picture) attached to the rotor fixture on the left.

The experimental campaign was carried out in Wind Tunnel A of the Chair of Aerodynamics and Fluid Mechanics of the Technical University of Munich (TUM-AER). The test section of this tunnel was 4.8 m long and its cross-section was 1.8 by 2.4 m. The turbulence intensity was below 0.4% in all three directions. The test bench on the rotating platform and outside views of the wind tunnel are shown on Figure 2. For load measurements, axes X and Y of the load cell correspond to in-plane axes of the propeller, whereas the Z axis represents the propeller rotation axis, as illustrated in Figure 2.

(**a**) (**b**)

Figure 2. (**a**) Test bench with Type A (APC) propeller blades positioned on the rotating platform in the wind tunnel, including axes adopted for load measurements. (**b**) Outside view of the TUM-AER Wind Tunnel A which was used for these experiments.

The load cell used had nominal maximum loads of 200 N/5 Nm in X and Y axes and 500 N/10 Nm in the Z axis. The motor used had a maximum power rating of 1955 W. Both of these components were each approximately 60 mm in diameter and 40 mm in length. The load cell was calibrated by the manufacturer and the measurement uncertainty

obtained during calibration was [0.016, 0.064, 1.380] N for forces and [0.006, 0.009, 0.003] Nm for moments in X, Y, and Z axes, respectively. Load data were collected at 3000 Hz, which resulted in a limit resolution frequency of 1200 Hz and maximum latency of 1.25 ms according to manufacturer data.

The power was supplied from the grid with an AC-DC converter delivering 48 V DC to the system. Control was achieved with an Electronic Speed Controller (ESC) from the same manufacturer as the motor and an Arduino PID (proportional–integral–derivative) controller with the three-phase ESC output in the feedback loop. A visual display indicating electric current and a temperature sensor for periodic measurements of the motor were used to monitor the motor status during the experimental campaign, because certain configurations required the motor to operate close to its limits.

Testing was aborted if either measured thrust was too close to zero, to avoid propeller windmilling, or if the monitoring of motor current and temperature indicated that the system was close to overheating. Loads were measured in static conditions and also at two different wind speeds, namely 10 and 25 m/s. Focus was placed on three different rotational speeds of the propellers—3000, 4000 and 5000 RPM—for which AoI sweeps from 0 (axial inflow) to 90 degrees were carried out. Some operating conditions, e.g., static axial inflow for two-bladed propellers were also measured at 2000 and 6000 RPM with the objective of comparing these results with previous measurements and the existing literature in order to validate the setup. Table 1 provides an overview of these testing conditions.

Table 1. Overview of testing conditions.

Wind Speed [m/s]	Motor RPM	Angle of Inflow (AoI)
0, 10, 25	2000–6000 (steps of 1000)	0–90° (steps of 15°)

Two different blade geometries were used for this measurement campaign. Figure 3 shows these blades and Table 2 contains information about manufacturer, number of blades, and pitch. All propellers had approximately the same diameter of 457 mm.

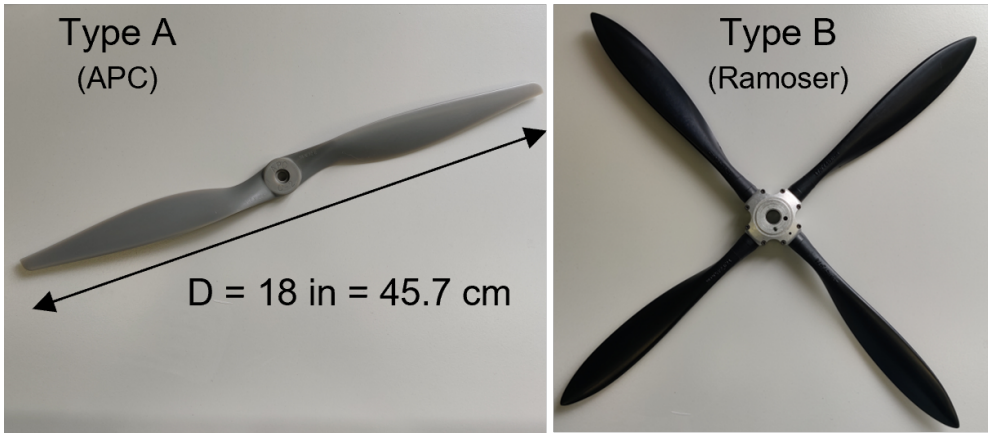

Figure 3. Different propeller types investigated. Type B (Ramoser) propeller enabled the measurement of the same blade geometry in 2-, 3-, 4-, and 5-bladed configurations.

In particular, Type B blades could be used with different hubs that allowed for adjustment of the blade number, enabling a direct assessment of the influence of blade number on propeller loads. Another interesting aspect of Type B propeller blades was that they do not have a predefined fixed pitch, so the pitch can be adjusted to be between 6 and 24 inches. However, a drawback to this flexibility was that the adjustment by hand was found to be imprecise and not easily repeatable. This may have led to slightly different pitch configurations between each blade mounted on a hub. An 8-channel amplifier was used to collect data from the load cell and temperature and optical sensors at 3000 Hz for 30 s, with all

channels measured simultaneously. Additionally, pressure and ambient temperature data were collected separately at 1 Hz and averaged over 10 s.

Table 2. Propeller types used in this investigation and their characteristics.

Type	Manufacturer	Blades	Diameter [in]	Pitch [in]
A	APC	2	18	[8, 12]
B	Ramoser	2, 3, 4, 5	17.95	[8, 12]

Experimental data were averaged in order to obtain aerodynamic coefficients. Performance of aircraft propellers under axial inflow is usually expressed in terms of thrust coefficient C_T and power coefficient C_P considering their variation over advance ratio J as defined by

$$C_T = \frac{T}{\rho n^2 D^4} \tag{1}$$

$$C_P = \frac{P}{\rho n^3 D^5} \tag{2}$$

$$J = \frac{V_\infty}{nD} \tag{3}$$

where ρ is air density, V_∞ is wind speed (inflow) and T, P, D and n are, respectively, propeller thrust, power, diameter, and rotational speed in rotations per second.

2.2. Numerical Approach

The implemented low-fidelity method was used to calculate propeller performance with axial inflow conditions, followed by non-axial conditions. The method is based on Blade Element Momentum Theory (BEMT), which is a well-known standard procedure to design or determine aerodynamic propeller performance within seconds.

The BEMT method was implemented as formulated in [19], and the governing equations for non-axial inflow conditions are given in [20] but are listed here as a quick reference. The quasi-steady aerodynamic forces of a propeller at non-axial inflow conditions were determined by solving the three non-linear equations with three unknowns a, a', and ϕ for every blade element at radius r and discrete azimuthal sector position θ, where a, a', and ϕ represent the axial and tangential interference factors and the flow angle. The rotational speed in [rad/s] is given by Ω. The equations are

$$\frac{a}{1+a} = \frac{\sigma\, C_y}{4F \sin^2 \phi} \tag{4}$$

$$\frac{a'}{1-a'} = \frac{\sigma\, C_x}{4F \cos\phi \sin\phi} \tag{5}$$

$$\phi = \arctan \frac{V_\infty \cos AoI (1+a)}{(V_\infty \sin AoI \sin\theta + \Omega r)(1-a')} \tag{6}$$

The sectional propeller solidity ratio σ offers the relation of radial propeller chord length c multiplied by the number of blades B and the respective circumferential length. It is defined by

$$\sigma = \frac{Bc}{2\pi\xi R} \tag{7}$$

where $\xi = r/R$ represents the blade element radial position with regard to total propeller radius R. Additionally,

$$C_x = C_L \sin\phi + C_D \cos\phi \tag{8}$$

$$C_y = C_L \cos\phi - C_D \sin\phi \tag{9}$$

represent the flow conditions at a blade section. Furthermore, the BEMT uses tip-loss factor F in a variant originally from [21] and also used by [22], which is

$$F = \frac{2}{\pi} \arccos\left[\exp -\frac{B(1-\xi)}{2\xi \sin\phi}\right] \tag{10}$$

Having the unknonws determined for each radial and azimuthal blade element, the partial derivatives of aerodynamic force coefficients, for example, for thrust coefficient C_T for a single blade, can be obtained as

$$\frac{\partial C_T(\xi,\theta)}{\partial \xi} = \frac{c\, C_y}{4n^2 D^3} \frac{V_\infty^2 \cos^2 AoI (1+a)^2}{\sin^2\phi} \tag{11}$$

The integral thrust coefficient C_T and all other force coefficients with regard to the propeller hub are obtained by integrating radial loading, given in Equation (11), at each azimuthal sector position θ and tracking all blades over a single revolution repeating this method in order to obtain the integral aerodynamic hub loading on the propeller over one rotation.

In contrast to most available open-source BEMT codes, the implemented method also considers azimuthal resolution and is therefore capable of tracing propeller loads over a rotation. This capability enables the calculation of propeller performance for non-axial inflow conditions. The advantage of the method is that it enables a very fast evaluation of results for several different parameters, such as number of blades, pitch settings, or RPM. Hence, it is well suited for a comparison with the results of the experimental study.

A blade geometry representation is provided in Figure 4 in terms of radial blade twist β and radial chord c given as chord-to-radius ratio c/R. The blade twist can also be described using pitch-over-diameter ratio p/D which directly relates to the design advance ratio J of the propeller blade. All these radial properties are shown over the non-dimensional propeller radius r/R.

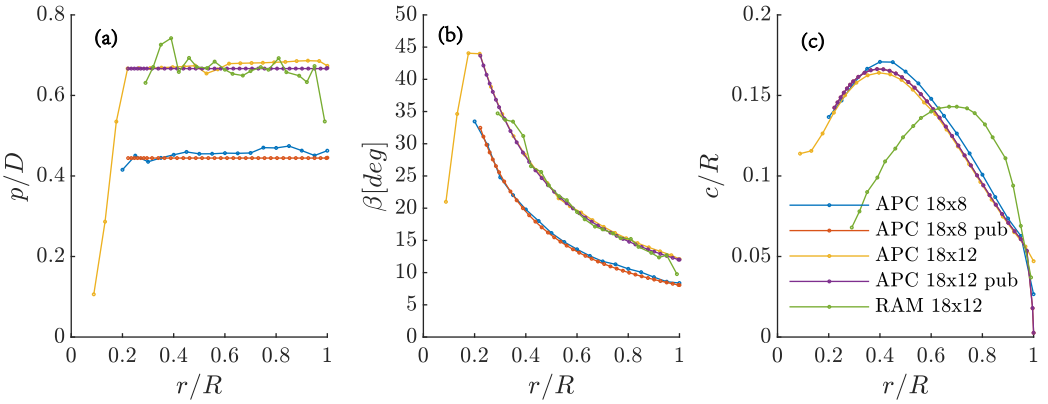

Figure 4. Comparison of radial blade geometry of APC 18×8E, APC 18×12E, and RAM 18×12 for extracted and published (pub) data by APC; In the figure, (**a**) radial pitch-to-diameter ratio, (**b**) radial blade twist, and (**c**) chord-to-diameter ratio; all data over non-dimensional blade radius r/R; published data for chord-to-diameter ratio of both APC blades overlap.

Furthermore, three radial airfoils at positions $xi = r/R = [0.35, 0.70, 0.95]$ are used to generate 2D polar data for the BEMT by means of CFD using a 2D-RANS approach.

The airfoil contours are shown in Figure 5 and polar data for the three different sections of the APC 18×8 propeller at various Reynold Numbers are presented in Figure 6.

While a CAD representation of Type A (APC 18×8E) propeller geometry was available from previous studies, the 18x12E variant was generated by adjusting the blade twist distribution based on manufacturer data. Type B (Ramoser) blade geometry had to be generated using a 3D scanner and extensive post-processing to smooth the measured geometry and extract blade section airfoils.

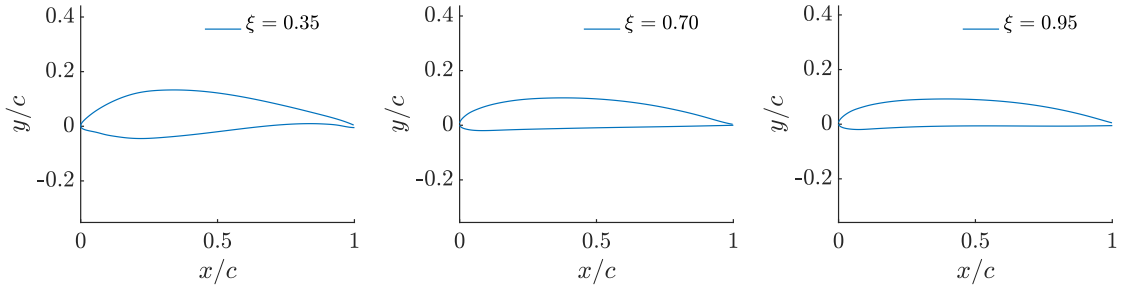

(**a**) Airfoil at $\xi = r/R = 0.35$ (**b**) Airfoil at $\xi = r/R = 0.70$ (**c**) Airfoil at $\xi = r/R = 0.95$

Figure 5. Three representative airfoil sections of APC 18×8E blade shape.

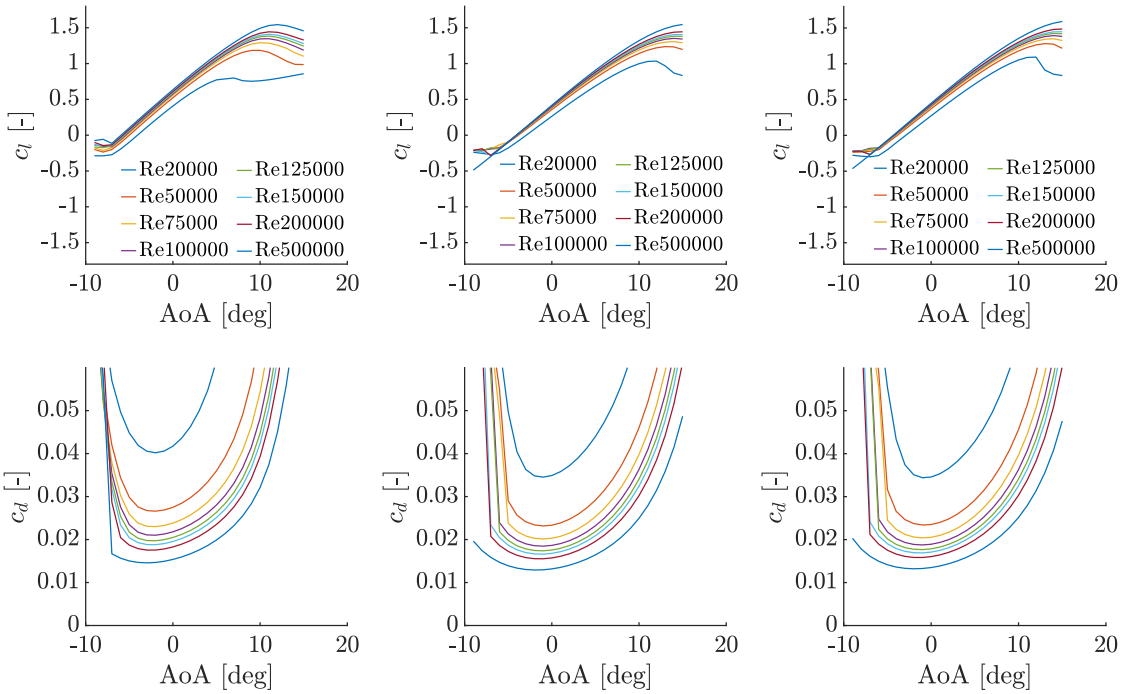

(**a**) Airfoil section at $\xi = 0.35$ (**b**) Airfoil section at $\xi = 0.70$ (**c**) Airfoil section at $\xi = 0.95$

Figure 6. Section-wise polar input obtained from 2D-RANS simulations for different Reynolds Numbers for APC 18×8E blade.

3. Results and Discussion

The results can be divided into three parts.

Initially, the time-averaged loads acting on the propellers are analyzed with axial inflow at different wind speeds, representing the propeller's performance data. This allows for validation of the test bench by comparison against the literature data and a comparison of experimental and BEMT results for traditional propeller operating conditions.

Then, the non-axial inflow conditions with an inflow angle of up to 90 degrees are considered. Experimental data are shown for force coefficients under various operating conditions, and a comparison over one propeller revolution is carried out between ex-

perimental and numerical results for different propellers at 15 degrees and 45 degrees of the inflow angle. This can offer insights into the transient load characteristics and their dependency on the number of blades.

Finally, oscillation amplitudes and frequencies for different propellers are analyzed, which is made possible by the experimental approach including time-resolved data acquisition.

3.1. Time-Averaged Results/Propeller Performance Data

The forces and moments obtained during the experimental campaign in the wind tunnel can be averaged and used to calculate aerodynamic coefficients for an analysis of the flow both in axial and non-axial conditions according to the equations previously described.

3.1.1. Axial Inflow

In order to validate the experimental setup, thrust and power coefficients at axial inflow for Type A (APC) propeller blades were compared with experimental data from [23]. The experimental, numerical (BEMT), and literature results can be seen in Figure 7.

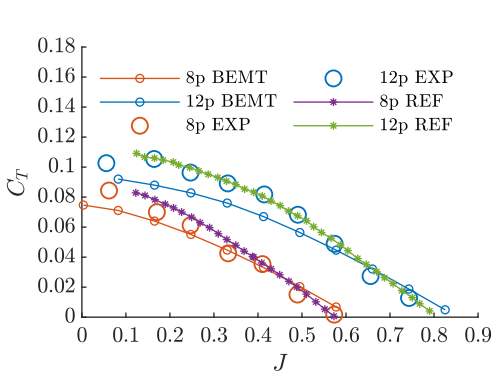

(**a**) APC 18x8E vs. 18x12E at 4000 RPM.

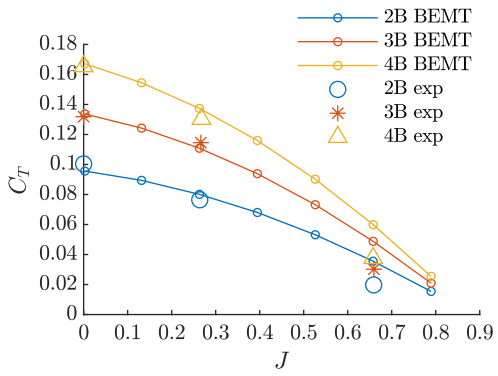

(**b**) RAM18x12 with 2,3,4 blades at 5000 RPM.

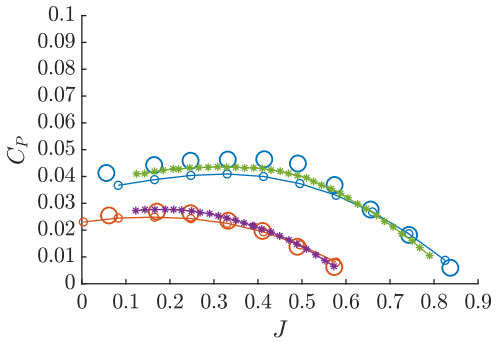

(**c**) APC 18x8E vs. 18x12E at 4000 RPM.

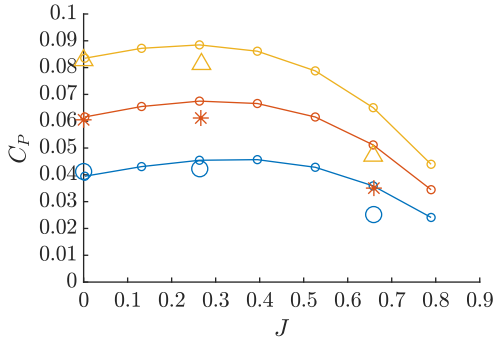

(**d**) RAM18x12 with 2,3,4 blades at 5000 RPM.

Figure 7. Thrust and power coefficients (C_T, C_P) over advance ratio J; REF data from [23].

Comparing results for both pitch settings of Type A (APC) propellers, there is good agreement between the currently reported experimental results and the experimental results in the literature, whereas BEMT results are slightly below the literature values, particularly at low advance ratios.

On the right side, the calculated Type B (Ramoser) two-, three-, and four-bladed propellers are compared to experimental data. The results show good agreement for lower advance ratios but an increased over-prediction over the experimental data for higher advance ratios above J = 0.4 for all three blade counts. Nevertheless, the dependency of blade number for these parameters was still captured by the BEMT method.

3.1.2. Non-Axial Inflow

Next, thrust and power coefficients of Type B (Ramoser) propellers are investigated for non-axial inflow conditions at two different inflow velocities with 5000 RPM; see Figure 8. The two-, three-, and four-bladed variants are considered for varying AoI from zero to 90° and results are compared against the experimental measurements. With regard to thrust coefficient, there is very good agreement between experimental and numerical results, both showing increasing thrust coefficient with AoI. BEMT results for 10 m/s wind speed show better agreement with experimental data, whereas for 25 m/s there is an over-prediction for $AoI < 40°$. Experimental results for thrust show a more accentuated slope over AoI for higher wind speed. Additionally, it is possible to identify that, for low AoI, thrust is decreased in comparison to static thrust values, but for high AoI there is an increase in thrust with inflow, and this change in behavior occurs between the measurement points of $AoI = [60°, 75°]$. This is in line with trends previously identified in experiments in [9,13,14]. Reference [14] provides a theoretical explanation for this phenomenon, suggesting that at high incidence angles, the propeller behaves similarly to an elliptic wing.

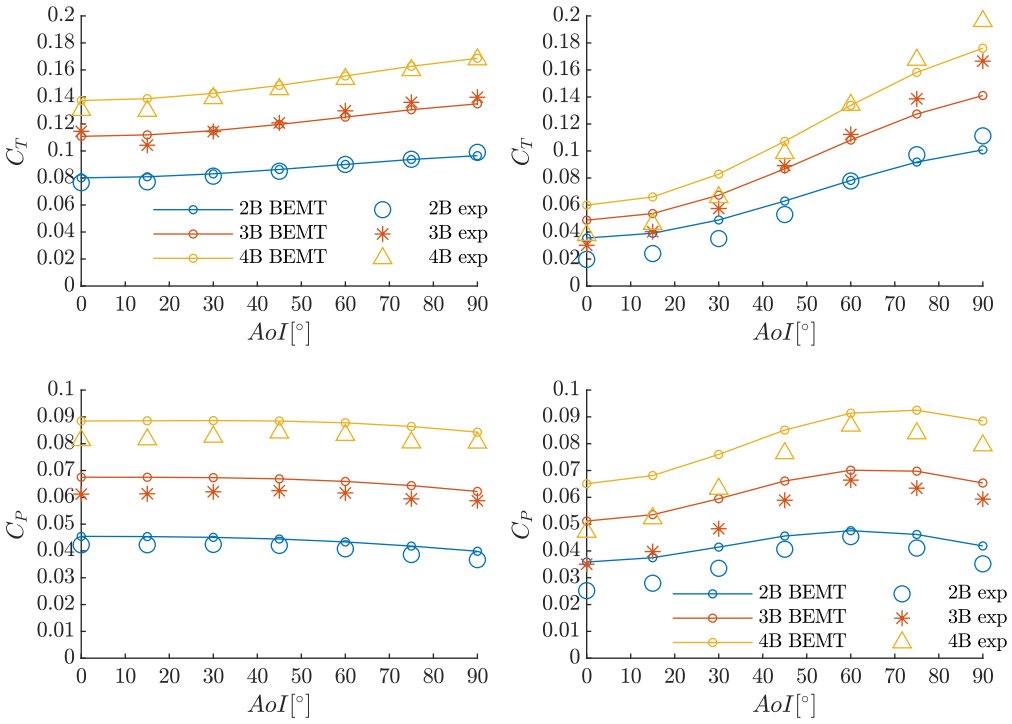

(**a**) Inflow of $V_\infty = 10$ m/s. (**b**) Inflow of $V_\infty = 25$ m/s.

Figure 8. Thrust and power coefficients, C_T and C_P, over AoA at $V_\infty = 10$ and 25 m/s with 5000 RPM; Type B propellers with 2, 3, and 4 blades.

With regard to power coefficient, again, there is better agreement between BEMT numerical and experimental results for 10 m/s wind speed than for 25 m/s, with a slight over-prediction of the numerical tool in the latter case. Nevertheless, for both wind speed conditions, the power coefficient trends are well represented numerically. For the lower wind speed, there is a strictly decreasing trend in power coefficient over AoI, whereas for the higher wind speed, the power coefficient increases from AoI 15 deg to 60 deg and decreases again for higher angles.

A direct consequence of flow asymmetry when considering propellers operating at an incidence angle to the incoming wind are additional forces acting in plane with the propeller disk (X and Y axes). Non-dimensional force coefficients C_X and C_Y can be

calculated similarly to the thrust coefficient, considering air density ρ, propeller rotational speed n, and diameter D as follows:

$$C_{X,Y} = \frac{F_{X,Y}}{\rho n^2 D^4} \tag{12}$$

Experimental results for time-averaged, integral in-plane force coefficients are shown in Figure 9 for the same propellers and operating conditions as in Figure 8. Absolute values are depicted to facilitate a comparison of force magnitude.

Results show that in-plane forces increase in magnitude with increasing AoI up to 75° for all blade counts, with a higher slope for a higher wind speed value. Additionally, the four-bladed variant resulted in higher average side force coefficients for the same rotational speed, although it is important to remember that this increase is accompanied by higher thrust coefficients as well.

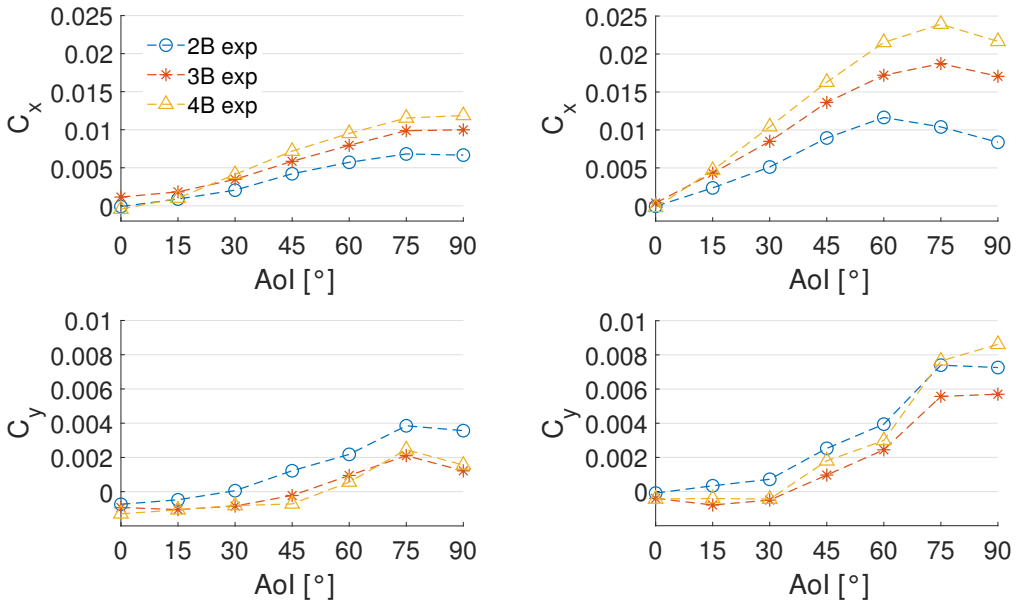

(**a**) Inflow of $V_\infty = 10$ m/s. (**b**) Inflow of $V_\infty = 25$ m/s.

Figure 9. Experimental force coefficients C_x and C_y over AoI for $V_\infty = [10, 25]$ m/s at 5000 RPM. Type B propellers with 2, 3, and 4 blades.

When considering in-plane forces and moments, advance ratio J as previously defined is not able to capture the AoI dependency of these aerodynamic quantities. Therefore, a definition of advance ratio μ similar to the one traditionally used in rotorcraft aerodynamics can be used considering the tangential component of inflow velocity for its calculation as follows:

$$\mu = \frac{V_\infty sin(AoI)}{2\pi n R} \tag{13}$$

with variables as previously defined and R as propeller radius. The decomposition of advance ratio in normal and tangential representations is also present in the literature [9,15]. Force coefficients for X and Y axes with regard to advance ratio μ at all different operating conditions of type B propellers are shown in Figure 10, including variations in RPM, pitch, number of blades and wind speed, and colored by experimental thrust coefficient.

The data in Figures 9 and 10 were corrected to remove the influence of the motor and mounting parts. This was achieved by running reference measurements with the test bench without the propeller blades (as shown in Figure 1) at the same wind speeds and

incidence angles and subtracting the forces measured in these reference situations from the measurements with propeller blades.

The data show a dependency of propeller in-plane average loads on advance ratio μ, whereas for an arbitrary advance ratio, the absolute magnitude of average lateral force coefficients increases as thrust increases.

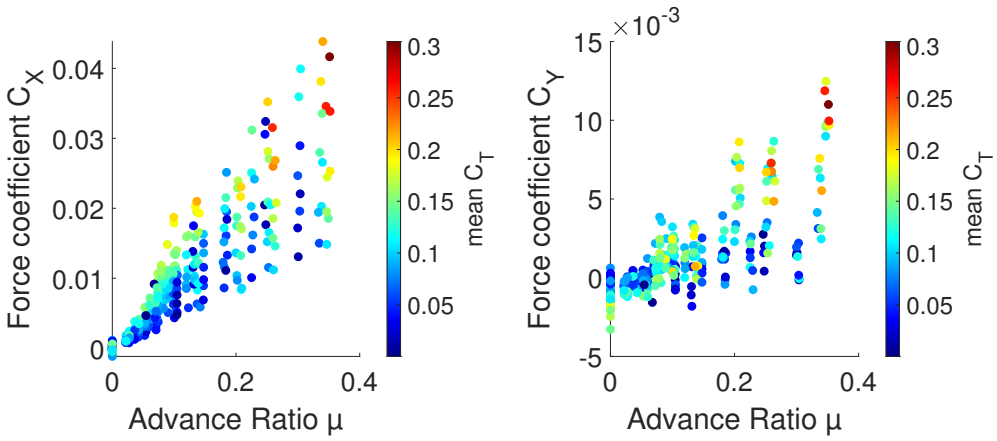

Figure 10. Lateral force coefficients C_X and C_Y for Type B (Ramoser) propeller blades, including variations in pitch, RPM, wind speed, and blade count. Experimental data.

3.2. Time-Resolved Results/Azimuthal Load Behavior

In this section, the mechanical hub loads of different propellers throughout a single rotation are analyzed.

Especially on the experimental side, time-resolved measurements represent a challenging task, since it is possible that structural parts of the test bench itself influence the measurements as they might affect the load cell by amplifying or dampening specific excitation frequencies. Nevertheless, the authors expect that repeating patterns identified with different propellers at different rotational speeds can be taken as an indication of transient load behavior, regardless of test bench influences.

The optical RPM sensor enables the calculation of a time-synchronous average of each load signal by overlapping the sections of the signal which correspond to one full rotation of the motor. Each of the black lines in Figure 11 is one such section, and the colored line is then the average of these individual sections over one rotation.

The data in Figure 11 are processed with a lowpass filter set at 800 Hz in order to enable better visualization of the first engine orders without including high-frequency oscillations, for example, the 14th engine order, which is present in all results and addressed later in Section 3.2.1.

Comparing the results for the two-bladed propellers at 0 and 90 degrees angle of inflow, it is noticeable that non-axial inflow leads to larger amplitudes of oscillation in measured forces in all three axes, with four visible peaks over one rotation. Now looking at a five-bladed propeller in the same operation and inflow conditions, although load oscillations are still visible, they are significantly lower in magnitude. A broader analysis of oscillation magnitude is provided in the next section.

One caveat of this analysis is that experimental data are obtained without a clear correlation to propeller azimuthal orientation, meaning the exact position of the blades is not known, only that a full rotation happened between two instances of the optical signal. Therefore, an attempt is made at aligning experimental data with BEMT results to enable a comparison by shifting all data by an equal step such that the moment around the Z axis (torque of the motor) agrees in the peak position with the BEMT data. The method allows at least for a comparison of measured load amplitudes and simulated results over one full rotation of the propeller.

Additionally, the experimental moment signals are corrected from the load cell reference system to a propeller-centered reference system with a simple translation of the origin of the system, considering the cross-product of measured forces with the lever arm between propeller and load cell.

An overlay of experimental results with BEMT results is provided in Figure 12. The BEMT coefficients of in-plane X-force and X-axis moment are compared from the two-bladed APC 18×12E (Type A) (left) and the three-bladed RAM 18×12 (Type-B) (right) at angles of incidence of $AoI = 15°$ and $AoI = 45°$.

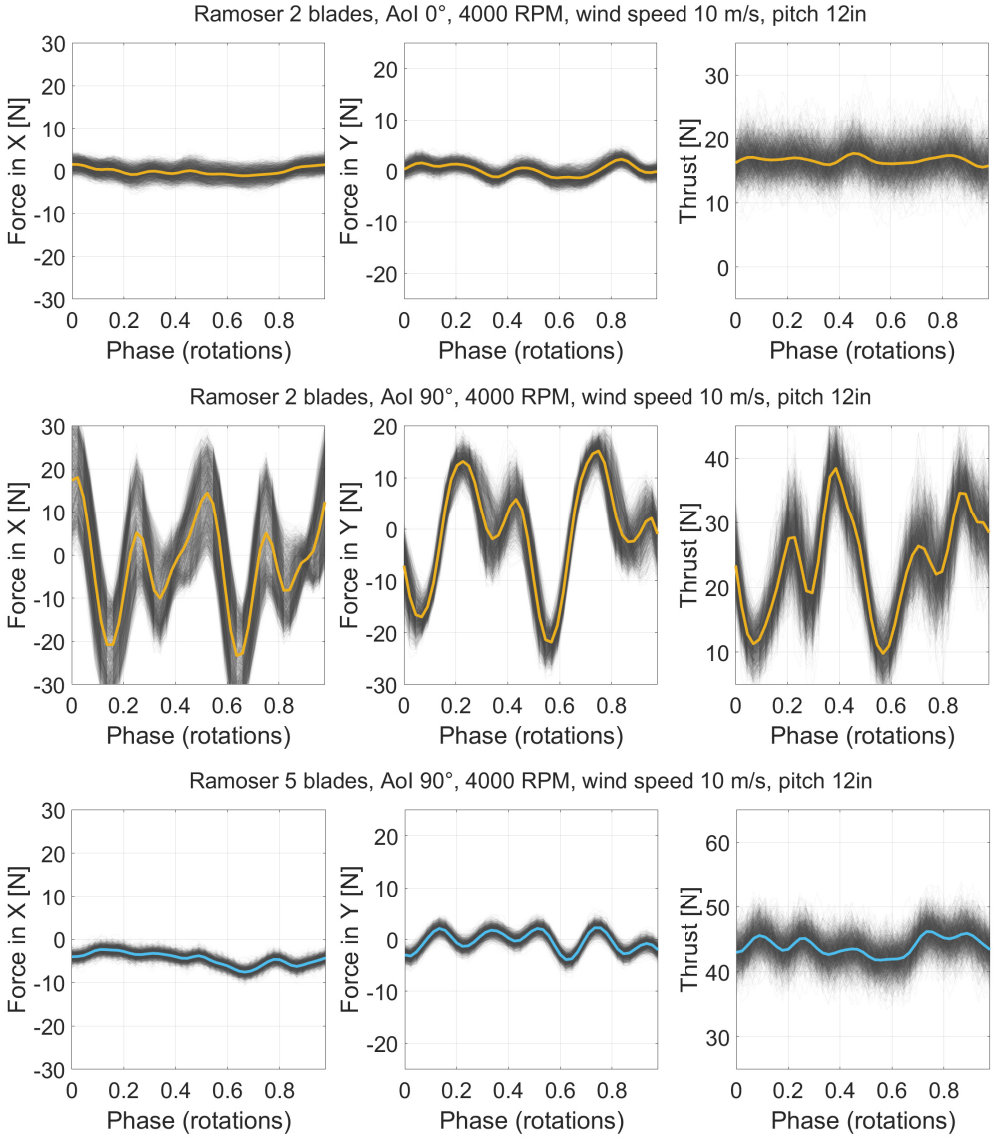

Figure 11. Experimental forces over one rotation for two Type B propellers at different incidence angles.

While BEMT results predict that the loads oscillate with a frequency directly related to the respective number of blades, amplitudes show strong deviation from experimental results, with experimental amplitudes higher than predicted by BEMT. Additionally, harmonic oscillations which were present in experimental results at high incidence angles, for example, as seen in Figure 12c, were not captured in BEMT results.

These results indicate that while the selected BEMT method can capture some asymmetric loading effects, it is still not able to predict oscillation amplitudes. Simulated results for 15° are closer to experimental results than for 45°, suggesting that the method is most reliable at smaller deviations from axial inflow. This is expected, since local flow detach-

ments and reverse flow especially at the retreating blade side can only be modeled using the respective input polar data.

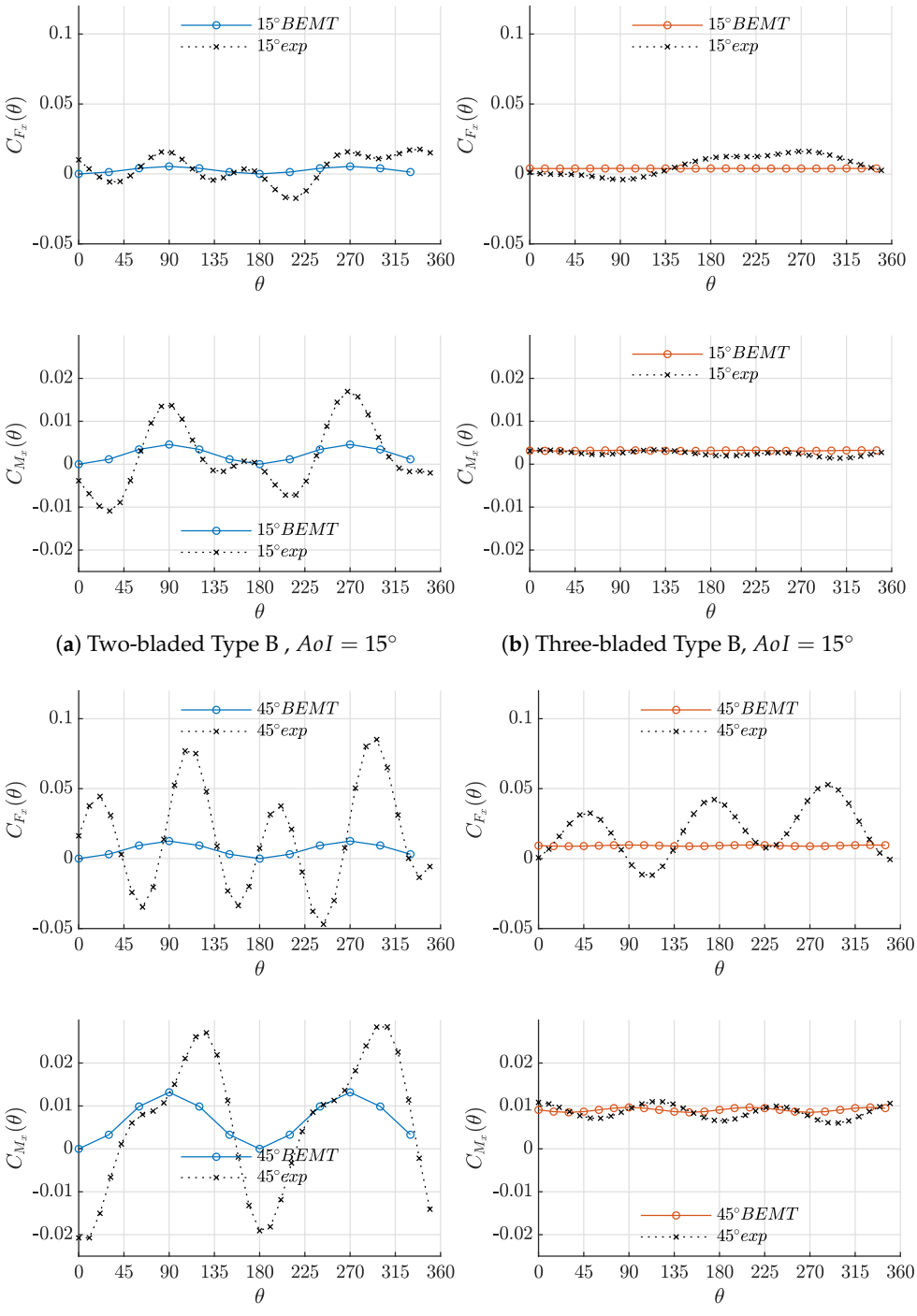

(**a**) Two-bladed Type B , $AoI = 15°$ (**b**) Three-bladed Type B, $AoI = 15°$

(**c**) Two-bladed Type B, $AoI = 45°$ (**d**) Three-bladed Type B, $AoI = 45°$

Figure 12. Experimental and BEMT results recorded over a single rotation for in-plane side force coefficient C_{F_x} and roll moment coefficient C_{M_x} for Type B propeller as a two-bladed variant (**left**) and a three-bladed variant (**right**); 5000 RPM at an inflow of $V_\infty = 25$ m/s; (**a**,**b**) at $AoI = 15°$; (**c**,**d**) at $AoI = 45°$.

3.2.1. Oscillation Amplitudes and Frequency Analysis

Average load values can only describe propeller aerodynamics and its resulting engineering challenges to a limited extent. The amplitudes and frequencies of the load

oscillations are also of great interest in this context, particularly considering structural design of vehicles with propellers that operate in non-axial flow conditions.

One way to compare the amplitude of the oscillatory behavior of the loads is to calculate Root Mean Square (RMS) values of zero-mean load signals. The load signals are shifted to oscillate around a mean value of zero in order to compare purely oscillatory behavior without including the differences in average magnitude of loads into the analysis.

Figure 13 shows RMS values for forces on three axes in relation to number of blades and angle of inflow considering all Type B (Ramoser) blade geometry experimental results, including variations in RPM, pitch, and wind speed. The data are color-coded by mean C_T in order to allow for a comparison of oscillatory behavior between propeller configurations with similar thrust performance.

These results suggest that there is a trend toward higher oscillation amplitudes for lower blade numbers and higher AoI. These results also indicate that propellers with lower number of blades show higher sensitivity to the asymmetry of inflow and consequent disparity in local angle of attack between individual blades attributed to non-axial inflow conditions. From a structural point of view, larger oscillation amplitudes of the loads could become problematic for the aircraft architecture.

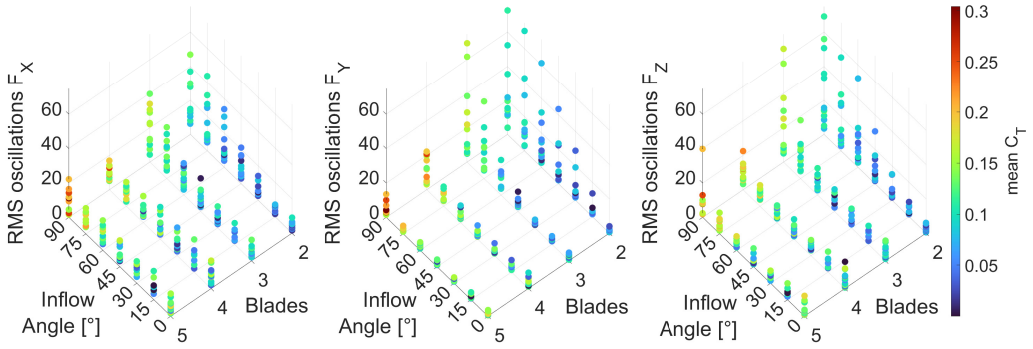

Figure 13. Experimental RMS values for the forces acting on the RAM propeller; measured for different propeller blade count and varying AoI , colored by experimental mean C_T. Results include different RPM, V_∞ and blade pitch configurations.

A frequency analysis of the results was also carried out. Figure 14 shows two Power Spectral Density (PSD) distributions for the same propeller in static (no wind) conditions and 25 m/s wind at a non-axial inflow angle of 90°. The engine orders are marked in red dashed lines to facilitate interpretation.

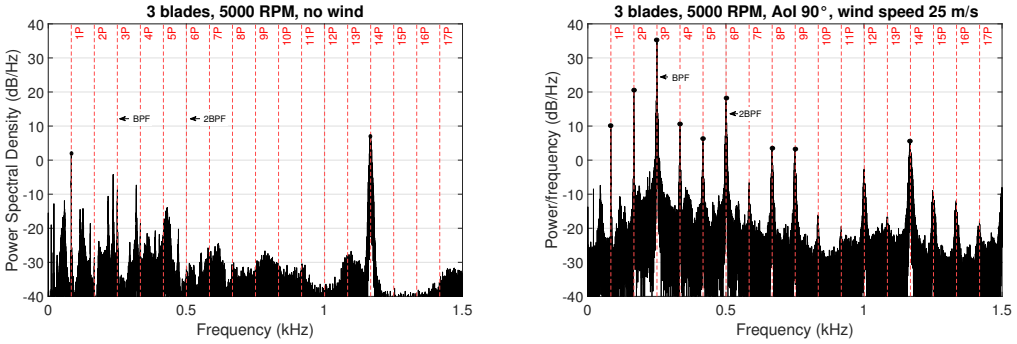

Figure 14. Power Spectral Density of lateral force F_y for Type B propeller with 3 blades, pitch 12 inches, 5000 RPM. Experimental data.

It is noticeable that the 14th engine order is present in a similar magnitude in both inflow conditions, although these conditions are extremely different from an aerodynamic perspective. In fact, an excitation of the 14th engine order was observed in all experimental

results with rotating propellers, regardless of varying parameters. This excitation is likely a result of an influence of the motor used, which had 28 poles.

Further, in static conditions, the dominant oscillating frequency is 1P (one per revolution), which is likely related to an imbalance of the propeller tested, whereas when the same propeller operates in non-axial inflow, the higher-order frequencies become relevant, especially Blade Passing Frequency (BPF) and twice the BPF, in this case 3P and 6P, but also many of its harmonics.

For a broader comparison of the influence of AoI, Figures 15 and 16 show PSD of lateral forces for AoI varying from 0 to 90 degrees for a two-bladed and a three-bladed propeller. The two charts in each figure show the same data in different views. On the left, each PSD is shown individually for different AoIs in order to provide an overview of the data being compared. On the right is a top view that allows for more detailed comparison and identification of the excited frequencies and how they relate to the engine orders.

Again, a clear dominance of the BPF can be seen, with higher magnitude at higher inflow angles. In addition, all harmonic frequencies also show amplitude peaks, indicating that not only the blade passing frequency but each harmonic of the rotational speed may be relevant for structural considerations. This last observation seems to be particularly crucial for the two-bladed propeller, since several results for two-bladed propellers at high AoI indicate that the double BPF (i.e., four times rotational frequency) is similar in magnitude or higher than BPF itself.

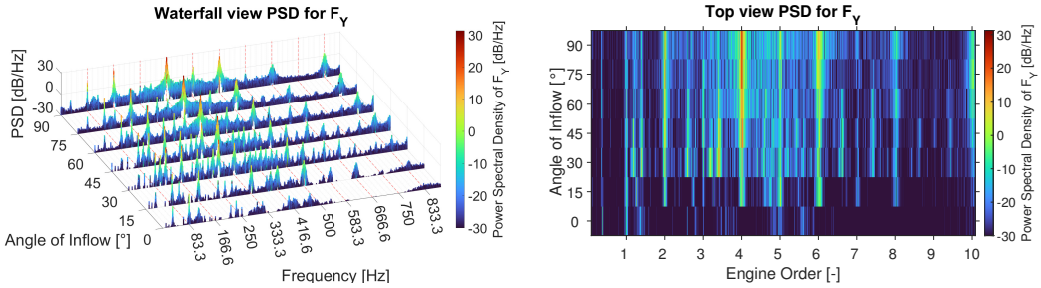

Figure 15. Type B (Ramoser) with two blades, 5000 RPM, pitch 12 inches, wind speed 25 m/s.

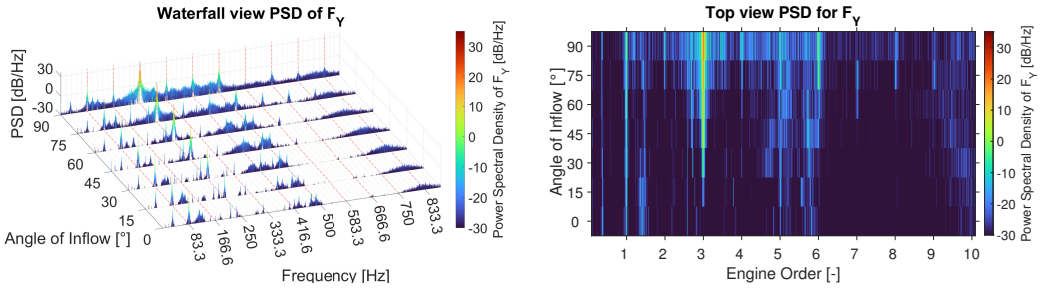

Figure 16. Type B (Ramoser) with three blades, 5000 RPM, pitch 12 inches, wind speed 25 m/s.

4. Conclusions

This work presented a comparison of experimental and numerical results regarding aero-mechanical fixed-pitch propeller loads under non-axial inflow conditions. A wind-tunnel propeller test bench for measuring unsteady load characteristics was described, and Type A propellers of different pitches as well as Type B propellers of different blade numbers were measured at both axial and non-axial inflow conditions. A Blade Element Momentum Theory (BEMT) method was used to compare results against wind-tunnel data. Experimental time-resolved data were also studied from the perspective of oscillation amplitudes and frequencies.

Results for 0° (axial) to 90° inflow angles were presented and can be summarized as follows:

- Average thrust and power coefficients for both axial and non-axial inflow with different pitch settings and blade numbers show good agreement between numerical BEMT prediction and experimental data, with better agreement at lower advance ratios.
- Thrust and side force coefficients C_T, C_X, and C_Y were shown to increase with the angle of inflow. Higher wind speed V_∞ resulted in steeper slopes.
- With all other parameters fixed, increasing inflow velocity results in increased thrust coefficients at very high angles of inflow (above circa 60°), opposite to propeller behavior at lower incidence angles. This result agrees with other experimental data in the literature.
- When resolved over one revolution of the propeller, numerical predictions showed oscillatory behavior dependent on blade number, as expected, but failed to predict correct amplitudes of oscillation for the loads.
- Amplitudes of oscillation of both thrust and in-plane forces were shown to increase with angle of inflow. Additionally, experimental oscillation amplitudes were higher for lower blade number propellers when operating in non-axial inflow.
- Frequency analysis of the results reveal that oscillations at BPF and its harmonics become increasingly significant with increasing angle of inflow. Harmonics seem to be more strongly excited for two-bladed propellers.

Testing techniques documented here can be applied to further expand the knowledge of propeller operation in non-axial inflow. Particularly the time-resolved approach can be used in future work to better understand oscillatory behavior of propeller loads in this scenario and its frequencies of interest. This information can be especially valuable for vehicle and component design and therefore progress in the UAM field.

Author Contributions: Conceptualization, C.M., N.H. and C.B.; methodology, C.M.; software, N.H.; formal analysis, C.M.; investigation, C.M. and N.H.; resources, C.B.; data curation, C.M.; writing—original draft preparation, C.M.; writing—review and editing, N.H.; visualization, C.M. and N.H.; supervision, C.B.; project administration, C.B.; funding acquisition, C.B. All authors have read and agreed to the published version of the manuscript.

Funding: This research was funded by the German Federal Ministry for Economic Affairs and Climate Action *(Bundesministerium für Wirtschaft und Klimaschutz)* within the LuFo VI-2 project ETHAN (Safe and Reliable Electrical and Thermal Networks for Hybrid-Electric Propulsion Systems), FKZ: 20L2103A, 20L2103B.

Data Availability Statement: The data presented in this study are openly available upon request.

Acknowledgments: The authors gratefully acknowledge the support of the Chair of Aircraft Design for the 3D scans required for the numerical methods, as well as the support of the students who assisted with measurements in the wind tunnel.

Conflicts of Interest: Author Nikolai Herzog was employed by the company Rolls-Royce Deutschland Ltd. & Co. KG. The remaining authors declare that the research was conducted in the absence of any commercial or financial relationships that could be construed as a potential conflict of interest.

Abbreviations

The following abbreviations are used in this manuscript:

AAM	Advanced Air Mobility
AoI	Angle of Inflow
BEMT	Blade Element Momentum Theory
BPF	Blade Passing Frequency
ESC	Electronic Speed Controller
eVTOL	Electric Vertical Take-Off and Landing
PID	Proportional–Integral–Derivative
PTFE	Polytetrafluoroethylene
RAM	Regional Air Mobility
RMS	Root Mean Square
RPM	Rotations per Minute
RPS	Rotations per Second
TUM-AER	Technical University of Munich, Chair of Aerodynamics and Fluid Mechanics
UAM	Urban Air Mobility
UAV	Unmanned Aerial Vehicle

References

1. Sheehan, V. *Vertical Flight Society Electric VTOL Aircraft Directory Reaches 700 Concepts*; Technical Report; Vertical Flight Society: Fairfax, VA, USA, 2022.
2. Garrow, L.A.; German, B.J.; Leonard, C.E. Urban air mobility: A comprehensive review and comparative analysis with autonomous and electric ground transportation for informing future research. *Transp. Res. Part C Emerg. Technol.* **2021**, *132*, 103377. [CrossRef]
3. Montagnani, D.; Tugnoli, M.; Fonte, F.; Zanotti, A.; Syal, M.; Droandi, G. Mid Fidelity Analysis of Unsteady Interactional Aerodynamics of Complex VTOL Configurations. In Proceedings of the 45th European Rotorcraft Forum, Warsaw, Poland, 17–20 September 2019.
4. Simmons, B.M.; Murphy, P.C. Wind Tunnel-Based Aerodynamic Model Identification for a Tilt-Wing, Distributed Electric Propulsion Aircraft. In Proceedings of the AIAA Scitech 2021 Forum; American Institute of Aeronautics and Astronautics, Virtual Event, 11–15 & 19–21 January 2021. [CrossRef]
5. Freeman, H.B. *The Effect of Small Angles of Yaw and Pitch on the Characteristics of Airplane Propellers*; NACA TR 389; US Government Printing Office: Washington, DC, USA, 1932.
6. Lesley, E.P.; Worley, G.F.; Moy, S. *Air Propellers in Yaw*; NACA TR 597; US Government Printing Office: Washington, DC, USA, 1937.
7. McLemore, H.C.; Cannon, M.D. *Aerodynamic Investigation of a Four-Blade Propeller Operating through an Angle-of-Attack Range from 0 to 180 Degrees*; NACA TN 3228; US Government Printing Office: Washington, DC, USA, 1954.
8. Gray, W.H.; Hallissy, J.M., Jr.; Heath, A.R., Jr. *A Wind-Tunnel Investigation of the Effects of Thrust-Axis Inclination on Propeller First-Order Vibration*; NACA TR 1205; US Government Printing Office: Washington, DC, USA, 1954.
9. Yaggy, P.F.; Rogallo, V.L. *A Wind-Tunnel Investigation of Three Propellers through an Angle-of-Attack Range from 0 deg to 85 deg*; NASA Ames Research Center Moffet Field, Technical Report TN-19890068078; US Government Printing Office: Washington, DC, USA, 1960.
10. Crigler, J.L.; Gilman, J., Jr. *Calculation of Aerodynamic Forces on an Inclined Dual-Rotating Propeller*; NACA RM L53D30; US Government Printing Office: Washington, DC, USA, 1953.
11. De Young, J. Propeller at high incidence. *J. Aircr.* **1965**, *2*, 241–250. [CrossRef]
12. Stratton, M.; Landman, D. Wind Tunnel Test and Empirical Modeling of Tilt-Rotor Performance for EVTOL Applications. In Proceedings of the AIAA Scitech 2021 Forum; American Institute of Aeronautics and Astronautics, Virtual Event, 11–15 & 19–21 January 2021. [CrossRef]
13. Leng, Y.; Jardin, T.; Bronz, M.; Moschetta, J.M. Experimental Analysis of Propeller Forces and Moments at High Angle of Incidence. In Proceedings of the AIAA Scitech 2019 Forum, San Diego, CA, USA, 7–11 January 2019. [CrossRef]
14. Rubin, R.L.; Zhao, D. New Development of Classical Actuator Disk Model for Propellers at Incidence. *AIAA J.* **2021**, *59*, 1040–1054. [CrossRef]
15. Simmons, B.M.; Hatke, D.B. *Investigation of High Incidence Angle Propeller Aerodynamics for Subscale eVTOL Aircraft*; Technical Report TM–20210014010; NASA Langley Research Center: Hampton, VA, USA, 2021.
16. Nguyen, V.B.; Rozehnal, D.; Hnidka, J.; Pham, V.U. Influence of yaw on propeller aerodynamic characteristics. *Eur. Phys. J. Web Conf.* **2018**, *180*, 02074. [CrossRef]
17. Cerny, M.; Faust, J.A.; Breitsamter, C. Investigation of a Coaxial Propeller Configuration Under Non-axial Inflow Conditions. In *New Results in Numerical and Experimental Fluid Mechanics XIII*; Series Title: Notes on Numerical Fluid Mechanics and Multidisciplinary Design; Dillmann, A., Heller, G., Krämer, E., Wagner, C., Eds.; Springer International Publishing: Cham, Switzerland, 2021; Volume 151, pp. 305–314. [CrossRef]
18. Faust, J.A.; Herzog, N.; Cerny, M.; Breitsamter, C. Development and Analysis of a Coaxial Rotor Test Bench in Axial Flow Conditions. In *New Results in Numerical and Experimental Fluid Mechanics XIII*; Series Title: Notes on Numerical Fluid Mechanics

and Multidisciplinary Design; Dillmann, A., Heller, G., Krämer, E., Wagner, C., Eds.; Springer International Publishing: Cham, Switzerland, 2021; Volume 151, pp. 335–344. [CrossRef]
19. Herzog, N.; Reeh, A. Implementation of a Method to Determine Aerodynamic Propeller-Wing Interaction. In *New Results in Numerical and Experimental Fluid Mechanics XII*; Series Title: Notes on Numerical Fluid Mechanics and Multidisciplinary Design; Dillmann, A., Heller, G., Krämer, E., Wagner, C., Tropea, C., Jakirlić, S., Eds.; Springer International Publishing: Cham, Switzerland, 2020; Volume 142, pp. 3–13. [CrossRef]
20. Cerny, M.; Herzog, N.; Faust, J.; Stuhlpfarrer, M.; Breitsamter, C. *Systematic Investigation of a Fixed-Pitch Small-Scale Propeller under Non-Axial Inflow Conditions*; Deutsche Gesellschaft für Luft- und Raumfahrt—Lilienthal-Oberth e.V.: Bonn, Germany, 2018. [CrossRef]
21. Betz, A. *Schraubenpropeller Mit Geringstem Energieverlust. Mit Einem Zusatz von l. Prandtl*; Nachrichten von der Gesellschaft der Wissenschaften zu Göttingen, Mathematisch-Physikalische Klasse: Göttingen, Germany, 1919; pp. 193–217.
22. Adkins, C.N.; Liebeck, R.H. Design of optimum propellers. *J. Propuls. Power* **1994**, *10*, 676–682. [CrossRef]
23. Dantsker, O.D.; Caccamo, M.; Deters, R.W.; Selig, M. Performance Testing of APC Electric Fixed-Blade UAV Propellers. In Proceedings of the AIAA AVIATION 2022 Forum, Chicago, IL, USA & Virtual, 27 June–1 July 2022; American Institute of Aeronautics and Astronautics: Reston, VA, USA, 2022. [CrossRef]